Binghe Liu
School for Engineering of Matter,
Transport and Energy,
Arizona State University,
Tempe, AZ 85287;
Department of Automotive Engineering,
School of Transportation Science and Engineering,
Beihang University,
Beijing, 100191, China;
Advanced Vehicle Research Center,
Beihang University,
Beijing, 100191, China

Xu Wang
School for Engineering of Matter,
Transport and Energy,
Arizona State University,
Tempe, AZ 85287

Hao-Sen Chen
Institute of Advanced Structure Technology,
Beijing Institute of Technology,
Beijing, 100081, China;
Beijing Key Laboratory of Lightweight
Multi-Functional Composite Materials and Structures,
Beijing Institute of Technology,
Beijing, 100081, China;
Collaborative Innovation Center
of Electric Vehicles in Beijing,
Beijing Institute of Technology,
Beijing, 100081, China

Sen Chen
Battery Business Unit,
Great Wall Motor Company Limited,
Baoding, 071000, China

Hongxin Yang
Battery Business Unit,
Great Wall Motor Company Limited,
Baoding, 071000, China

Jun Xu[1]
Department of Automotive Engineering,
School of Transportation Science and Engineering,
Beihang University,
Beijing, 100191, China;
Advanced Vehicle Research Center,
Beihang University,
Beijing, 100191, China
e-mail: junxu@buaa.edu.cn

Hanqing Jiang[1]
School for Engineering of Matter,
Transport and Energy,
Arizona State University,
Tempe, AZ 85287
e-mail: hanqing.jiang@asu.edu

Dai-Ning Fang
Institute of Advanced Structure Technology,
Beijing Institute of Technology,
Beijing, 100081, China;
Beijing Key Laboratory of Lightweight
Multi-Functional Composite Materials and Structures,
Beijing Institute of Technology,
Beijing, 100081, China;
State Key Laboratory for Turbulence and Complex Systems,
College of Engineering,
Peking University,
Beijing, 100871, China

A Simultaneous Multiscale and Multiphysics Model and Numerical Implementation of a Core-Shell Model for Lithium-Ion Full-Cell Batteries

The increasing significance on the development of high-performance lithium-ion (Li-ion) batteries is calling for new battery materials, theoretical models, and simulation tools. Lithiation-induced deformation in electrodes calls attention to study the multiphysics coupling between mechanics and electrochemistry. In this paper, a simultaneous multiscale and multiphysics model to study the coupled electrochemistry and mechanics in the continuum battery cell level and the microscale particle level was developed and implemented in COMSOL MULTIPHYSICS. *In the continuum scale, the porous electrode theory and the classical mechanics model were applied. In the microscale, the specific particle structure has been incorporated into the model. This model was demonstrated to study the effects of mechanical constraints, charging rate, and silicon/C ratio, on the electrochemical performance. This model provides a powerful tool to perform simultaneous multiscale and multiphysics design on Li-ion batteries, from the particle level to full-cell level.*
[DOI: 10.1115/1.4042432]

Keywords: lithium-ion batteries, multiscale, multiphysics, finite element simulations

[1]Corresponding authors.
Contributed by the Applied Mechanics Division of ASME for publication in the JOURNAL OF APPLIED MECHANICS. Manuscript received November 27, 2018; final manuscript received December 24, 2018; published online January 30, 2019. Editor: Yonggang Huang.

1 Introduction

The importance of low-cost, high-performance electrical energy storage systems has become increasingly significant in recent years by the need to accelerate the adoption of electrical vehicles and ubiquitous portable devices. Consequently, increasing the energy density of current commercial lithium-ion (Li-ion) batteries has become an important and extensively pursued research topic. Silicon (Si) is an attractive anode material being closely scrutinized for use in Li-ion batteries because of its highest-known theoretical charge capacity of 4200 mAh/g, more than 10 times higher than the current graphite anode Boukamp et al. [1]. However, comparing to the traditional graphite anode, both Si-containing anode and pure Si anode lead to large volumetric expansion during lithiation, which may cause the particle cracking [2–4], failure of adhesives [5,6], and solid electrolyte interface [7], as well as the stress of the electrode and separator [8].

Encouraged by the promising application of Si-containing anode, many new technologies have been explored to advance Si as a practical anode for Li-ion batteries, such as Si nanowires [9], Si nanoparticles [10], Si nanocomposites [11,12], Si nanotubes [13], and Si thin films [14,15]. Many theoretical models have been developed to understand the multiphysics of Li-ion batteries, particularly for Si-containing anodes where large elastic-plastic deformation and fracture present. Christensen and Newman [16] developed a mathematical model to calculate lithiation-induced volumetric expansion and stress evolution, considering the effect of pressure-driven diffusion and nonideal interactions between Li and host materials. Finite deformation models were used to study the coupling effect of two-way coupling between diffusion and stress [17,18]. Coupled electrochemical-thermal-mechanical models have been developed [19]. Plastic deformation [20], anisotropic [21], and phase-separation [22,23] of Si-based anodes were also studied. Furthermore, Si particle fracture during diffusion caused by the diffusion-included stress was investigated [24–26]. Stress, diffusion, and deformation coupled models have been utilized to study the lithiation behaviors of particles with different morphologies [27,28], electrical operations [29,30], and mechanical loadings [31]. Large-scale simulations (e.g., cell scale) to study the mechanical–electrochemical behavior of the batteries using reconstructed microstructures [32,33] and homogenization method [34,35] were conducted.

To the best of our knowledge, there is no simultaneous multiscale and multiphysics model to capture the mechanical–electrochemical behavior of the battery cells from the particle scale with details of different particle morphologies and compositions to cell scales with different mechanical and electrochemical boundary conditions. Specifically, many models just focus on the multiphysics coupling in one scale, such as in either particle scale (e.g., see Refs. [36] and [37]) or thin film electrode scale (e.g., see Ref. [37]), without multiscale coupling. Some efforts have been attempted to combine the multiscale and multiphysics by including multiple particles in the electrode [38–40], which may lead to expensive computational costs.

In this paper, we develop an efficient model to simultaneously study the multiscale and multiphysics of Li-ion full-cell (contains all the basic battery components, e.g., anode, cathode, separator, and battery casing) batteries where fully coupled electrochemistry and mechanics is considered in both scales and physics. In Sec. 2, we first develop the multiscale and multiphysics model based on the classical pseudo two-dimensional electrochemical model [41,42] to describe the electrochemical-mechanical coupling behavior both in the cell scale (i.e., continuum level) and the particle scale (i.e., the microscale level). Four specific models are adopted to describe the multiphysics behaviors in different scales. To demonstrate this model, various charging and casing conditions are considered in the continuum scale and a core-shell particle structure is used in the microscale. The following field variables will be captured in this model. In the continuum scale, the electrochemical potential, Li concentration, and stress/strain and deformation of anode and cathode will be computed. In the microscale, Li concentration, stress/strain, and deformation of the active particles will be obtained. For Si-anode anode, large deformation is considered. COMSOL MULTIPHYSICS will be utilized to implement this model, where the microscale model is executed through extra dimension nodes method. Typical results will be given in Sec. 3. The influence of practically important design parameters for Li-ion batteries (e.g., battery casing that providing mechanical constraints, charging schemes, and Si/C ratio in the microscale) will be addressed in Sec. 4, followed by concluding remarks in Sec. 5.

2 A Multiscale and Multiphysics Model

Figure 1 shows the schematic of the simultaneous multiscale and multiphysics model. This quad chart-liked schematic shows the key field variables and the nature of coupling. Field variables in the continuum scale are represented by capitalized letters and those in the microscale are written in lower-case letters. In the continuum scale, electrochemistry-related field variables are potential in the solid (i.e., anode and cathode) Φ_s, potential in the electrolyte Φ_e, and Li^+ concentration in the electrolyte C_e; and mechanics-related field variables are stress Σ_{ij} and strain Ψ_{ij}. The coupling in the continuum scale is to pass the average Li concentration c_s^{ave} from the electrochemical model to the mechanics model, which introduces lithiation-induced eigen expansion in the mechanics model. In the microscale, the electrochemical field variable is Li concentration in the particle c_s; and mechanics model captures hydrostatic stress σ_h and particle deformation u. The coupling in the microscale is to pass the Li concentration c_s from the electrochemical model to the mechanics model that leads to eigen deformation in the mechanics model. In addition to the multiphysics coupling, the following multiscale couplings are considered. The electrochemical model in the continuum scale couples with its counterpart in the microscale by passing the intercalation reaction current density I that affects Li^+ flux on the surface of the particle in the microscale; and the reverse coupling is achieved by passing the surface Li concentration (in the particle c_s^{surf}) from the microscale to the continuum scale model that determines the open circuit potential (OCP) of the electrode in the continuum model. The mechanics model in the continuum scale passes deformation gradient $\mathbf{F}$ to the microscale mechanics model to determine the localized deformation.

This model forms a closed loop to simultaneously study the multiscale and multiphysics behavior of Li-ion full cells. For one scenario, Li-ion batteries with different mechanical constraints (e.g., different casing conditions) under the same electrochemical conditions (e.g., charging rate), will generate different stress and strain in the continuum scale, which will be passed to the microscale where the mechanics and electrochemistry in the particles are coupled. Different stress and deformation in the particles will lead to different surface Li concentration, which in turn determines the electrochemical potential in the continuum scale and show as the open circuit potential of the battery cell. Finally, the average Li concentration further affects the stress/strain in the continuum scale and forms a closed loop. In this scenario, mechanics and electrochemistry form a two-way strong coupling with the influence from the microscale structure to the performance of the battery full cells in the continuum scale.

In this section, the governing equations for each level and the corresponding physics will be described.

2.1 Electrochemical Model in the Continuum Scale. The porous electrode theory [41,42] was used to describe the electrochemistry in the continuum scale and is briefly provided here. The porous electrode theory considers electrolyte thoroughly wetting the cathode and anode through the pores, and thus superimposes the electrolyte and electrodes as continua. Electrolyte and electrodes are liquid and solid phases in the superimposed continua, respectively. This theory has three fundamental field variables,

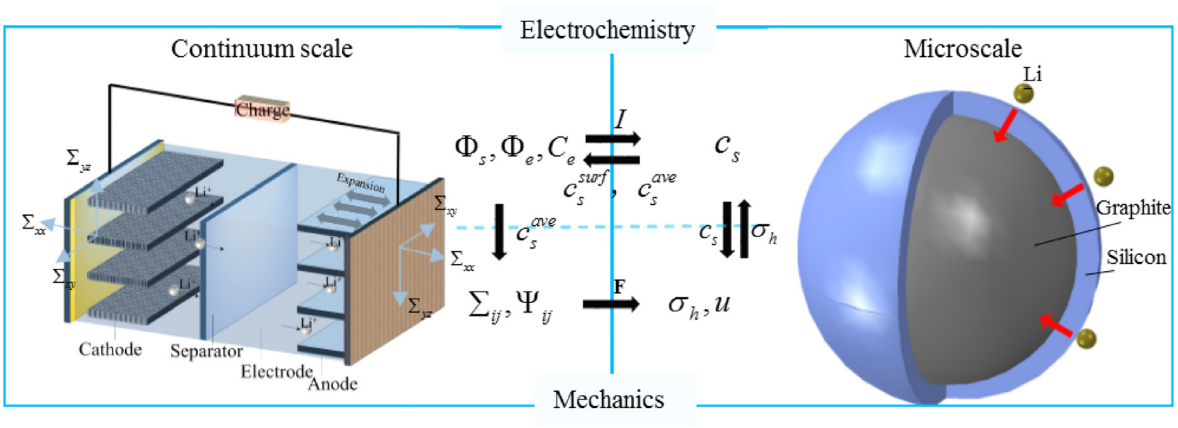

Φ_s : potential in the solid phase

Φ_e : potential in the liquid phase

C_e: Li^+ concentration in the liquid phase

Σ_{ij}: stress in the continuum scale

Ψ_{ij}: strain in the contimuum scale

F: deformation gradient in the contimuum scale

c_s: Li concentration in the particle

c_s^{surf}: The surface Li concentration in the particle

I: intercalation reaction current density

σ_h : hydrostatic stress in microscale

u: radial displacement in microscale

c_s^{ave}: average Li concentration

Fig. 1 Illustration of the present multiscale and multiphysics models. Key field variables and the way of coupling across two physics (i.e., electrochemistry and mechanics) and two scales (i.e., battery cell in the continuum scale and particles in microscale) are presented.

namely potential in the solid phase (i.e., anode and cathode) Φ_s, potential in the liquid phase Φ_e, and Li^+ concentration in the liquid phase C_e.

The intercalation occurs at the solid/liquid interface with current density I, which can be given by the Bulter–Volmer equation, i.e.,

$$I = I_0\left\{\exp\left[\frac{\alpha_a F\eta}{RT}\right] - \exp\left(-\frac{\alpha_c F\eta}{RT}\right)\right\} \tag{1}$$

Here, I_0 is the exchange current density and η is the overpotential, which are given by

$$I_0 = Fk_c^{\alpha_a}k_a^{\alpha_c}\left(c_s^{\max} - c_s^{\text{surf}}\right)\left(c_s^{\text{surf}}\right)^{\alpha_c}\left(\frac{C_e}{C_e^{\text{ref}}}\right)^{\alpha_a} \tag{2}$$

$$\eta = \Phi_s - \Phi_e - E_{\text{ref}}\left(c_s^{\text{surf}}\right) \tag{3}$$

where F is Faraday's constant, R is the gas constant, T is the temperature, k_c is the cathodic rate constant, k_a is the anodic rate constant, α_c is the cathodic transfer coefficient, α_a is the anodic transfer coefficient, c_s^{surf} is the surface Li concentration in the particle passed by the microscale model, $c_s^{\max}$ is the maximum Li concentration in the particle, C_e^{ref} is the reference value of Li^+ concentration in the electrolyte, E_{ref} is the OCP as a function of c_s^{surf}. Here, subscript "s" represents the solid phase in the superimposed continua. For composite electrodes with i-substances, such as a composite silicon (Si)/C anode electrode, $c_{s,i}$ is used to describe the Li concentration in the ith substance.

In the superimposed continua, there are two charge currents, namely current density $\mathbf{I}_e$ for the liquid phase and $\mathbf{I}_s$ for the solid phase, and one Li^+ flux density $\mathbf{J}_e$ for the liquid phase. The conservation of charges and mass defines the equilibrium equations

$$\nabla\cdot\mathbf{I}_e = a_s I \tag{4}$$

$$\nabla\cdot\mathbf{I}_s = -a_s I \tag{5}$$

$$\varepsilon_e\frac{\partial C_e}{\partial t} = -\nabla\cdot\mathbf{J}_e + \frac{a_s I}{F} \tag{6}$$

Here, $a_s = 3\varepsilon_s/r_p$ is the active surface area per unit electrode volume, where ε_e and ε_s are the volume fraction of the liquid and solid phases in the superimposed continua, respectively; r_p is the radius of the particle.

The kinetics of the current density and Li^+ flux density is given by the gradient of potential and/or concentration. In the liquid phase of the superimposed continua, the current density $\mathbf{I}_e$ and the lithium flux density $\mathbf{J}_e$ are given by

$$\mathbf{I}_e = -\kappa_e^{\text{eff}}\left[\nabla\Phi_e - \frac{2RT}{F}\left(1 + \frac{d\ln f_{\pm}}{d\ln C_e}\right)(1 - t_+)\nabla\ln C_e\right] \tag{7}$$

$$\mathbf{J}_e = -D_e^{\text{eff}}\nabla C_e + \frac{t_+}{F}\mathbf{I}_e \tag{8}$$

where both the potential gradient- and concentration gradient-driven mechanisms are included. In the solid phase of the superimposed continua, the current density $\mathbf{I}_s$ is given by

$$\mathbf{I}_s = -\kappa_s^{\text{eff}}\nabla\Phi_s \tag{9}$$

which is driven by the potential gradient. The involved material parameters are: the effective electrical conductivity of the liquid phase $\kappa_e^{\text{eff}} = \kappa_e\varepsilon_e^{1.5}$ with κ_e as the electrical conductivity of the electrolyte, the molar activity coefficient $1 + (d\ln f_{\pm}/d\ln C_e)$ to account for deviations from ideal behavior in a mixture of chemical substances, the transfer data t_+ as the fraction of the total electrical current carried by Li^+ in an electrolyte, the effective Li^+ diffusion coefficient of the liquid phase $D_e^{\text{eff}} = D_e\varepsilon_e^{1.5}$ with D_e as the Li^+ diffusion coefficient in the electrolyte, and the effective electrical conductivity of the solid phase $\kappa_s^{\text{eff}} = \kappa_s\varepsilon_s^{1.5}$ where κ_s is the electrical conductivity of the solid.

The electrochemistry model in the continuum scale can be implemented in COMSOL MULTIPHYSICS via its Li-ion battery module. Given that the battery cell does not have large deformation during charging/discharging and mechanical loading, it is not necessary to differentiate undeformed and deformed states, and thus all variables are just true variables.

2.2 Mechanics Model in the Continuum Scale. The classical equilibrium is used, $\nabla\cdot\boldsymbol{\Sigma} = 0$, where $\boldsymbol{\Sigma}$ is the stress in the

continuum scale. The electrodes are modeled as linear elastic isotropic materials with the constitutive relations as $\Sigma_{ij} = K_{ijkl}(\Psi_{kl} - \Psi_{\text{eigen}}\delta_{kl})$, where K_{ijkl} is the effective stiffness tensor of the electrodes, Ψ_{kl} is the strain, and Ψ_{eigen} represents the intercalation-induced eigen strain

$$\Psi_{\text{eigen}} = \alpha \Delta c_s^{\text{ave}} \tag{10}$$

Here, α is the coefficient of lithiation expansion and c_s^{ave} is the average Li concentration. For a composite electrode, rule of mixture can be used to determine the average Li concentration, which in turn determines α. Specifically, the average Li concentration for a Si/C anode with Si/C volume ratio γ is given by $\Delta c_s^{\text{ave}} = \gamma \Delta c_{s,\text{Si}}^{\text{ave}} + (1-\gamma)\Delta c_{s,\text{C}}^{\text{ave}}$, and effective partial molar volume Ω_{eff} can be given by $\Omega_{\text{eff}} = (\Omega_{\text{Si}}\gamma \Delta c_{s,\text{Si}}^{\text{ave}} + \Omega_C(1-\gamma)\Delta c_{s,\text{C}}^{\text{ave}}/\Delta c_s^{\text{ave}})$, where Ω_{Si} and Ω_C are partial molar volume of Si and C, respectively. Thus, the coefficient of lithiation expansion α is obtained as

$$\alpha = \frac{\sqrt[3]{1 + \Omega_{\text{eff}} \Delta c_s^{\text{ave}}} - 1}{\Delta c_s^{\text{ave}}} \tag{11}$$

The mechanics model in the continuum scale can be implemented in COMSOL MULTIPHYSICS via its solid mechanics module. For the same reason, as in electrochemistry model in the continuum scale, all variables in this model are just true variables.

2.3 Electrochemistry in the Microscale. Nominal variables, that are defined based on undeformed state, are used in the microscale model given that Si-containing electrodes have large deformation. Specifically, c_s is the nominal Li concentration in the particle, $\mathbf{j}_s$ is the nominal Li flux, and $\mathbf{x}$ is the undeformed coordinate. For the composite electrode (e.g., Si/C anode), there are more than one substance in the electrode. It is necessary to differentiate variables in each substance, such as $c_{s,\text{Si}}$ and $j_{s,\text{C}}$. However, to make the text concise, we do not specifically differentiate substances in the governing equations that are in fact applied to individual substance.

The conservation of Li in a particle is given by

$$\frac{\partial c_s}{\partial t} + \frac{\partial \mathbf{j}_s}{\partial \mathbf{x}} = 0 \tag{12}$$

and $\mathbf{j}_s$ is related to the gradient of chemical potential via

$$\mathbf{j}_s = -M c_s \frac{\partial \mu}{\partial \mathbf{x}} \tag{13}$$

where M is the mobility of Li and μ is the chemical potential of Li in a substance. The chemical potential is written as

$$\mu = \mu(c_s) - \Omega \sigma_h \tag{14}$$

where $\mu(c_s)$ is the Li concentration dependent chemical potential, Ω is the partial molar volume for each substance (i.e., Ω_{Si} and Ω_C), and $\sigma_h = (1/3)\text{tr}(\boldsymbol{\sigma})$ is the hydrostatic pressure. The chemical potential $\mu(c_s)$ relates to the open circuit potential E_{ref} via

$$\mu(c_s) = \mu(\text{Li}) - F E_{\text{ref}} \tag{15}$$

where $\mu(\text{Li})$ is the chemical potential of Li metal. The mobility M is related to the Li concentration and can be written as

$$M = M_0 \left(1 - \frac{c_s}{c_s^{\max}}\right) \tag{16}$$

where $M_0 = D_0/RT$ is the lithium mobility in the solid with dilute lithium concentration, and D_0 is the lithium diffusion in solid (e.g., Si or C).

For the spherical particles, the general governing Eqs. (12)–(16) can be degenerated to a spherical symmetry problem using r as the coordinate in the radial direction in an undeformed configuration. For example, the conservation law (i.e., Eq. (12)) becomes

$$\frac{\partial c_s}{\partial t} + \frac{1}{r^2}\frac{\partial (r^2 j_s)}{\partial r} = 0 \tag{17}$$

To implement the electrochemistry in the microscale along its counterpart in the continuum scale, extra dimension nodes method was used [43]. Extra dimension nodes are chosen from the continuum model and each extra dimension node carries the electrochemical variables (e.g., intercalation current I) and mechanics variables (e.g., deformation gradient $\mathbf{F}$) from the continuum model, and is governed by the governing equations in the microscale (i.e., Eqs. (12)–(17)), as shown in Fig. 2. The extra dimension nodes method is implemented in COMSOL MULTIPHYSICS via its weak form of the governing equations. By introducing a test function $\hat{c}_s$, the weak form of Eq. (17) is given by

$$\int_r \left(\frac{\partial c_s}{\partial t} + \frac{1}{r^2}\frac{\partial r^2 j_s}{\partial r}\right)\hat{c}_s dr = 0 \tag{18}$$

The detailed structure of the particle now can be captured. For example, the C-core and Si-shell structure can be reflected by performing the integration of Eq. (18) in individual C and Si domains. It should be emphasized here that r is the coordinate in the radial direction defined in the undeformed state; and thus, these equations are evaluated in the undeformed state while the concentrations (i.e., c's) are nominal variables. For C-core with radius r_C, Eq. (18) becomes

$$\int_0^{r_C} \left(-r^2 \frac{\partial c_{s,C}}{\partial t}\hat{c}_{s,C} + r^2 A_C \frac{\partial c_{s,C}}{\partial r}\frac{\partial \hat{c}_{s,C}}{\partial r} + r^2 B_C \frac{\partial \sigma_{h,C}}{\partial r}\frac{\partial \hat{c}_{s,C}}{\partial r}\right) dr = r^2 \hat{c}_{s,C}\left(A_C \frac{\partial c_{s,C}}{\partial r} + B_C \frac{\partial \sigma_{h,C}}{\partial r}\right)_0^{r_C} \tag{19}$$

where

$$A = \frac{D_0 F}{RT}\left(\frac{c_s}{c_s^{\max}}\right)(c_s^{\max} - c_s)\frac{\partial E_{\text{ref}}}{\partial c_s} \tag{20}$$

$$B = \frac{D_0}{RT}\left(\frac{c_s}{c_s^{\max}}\right)(c_s^{\max} - c_s)\Omega \tag{21}$$

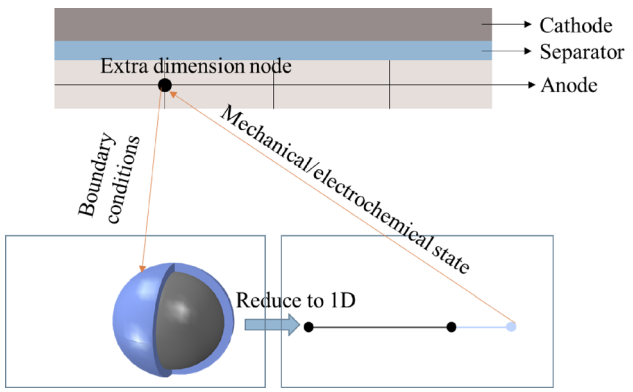

Fig. 2 Illustration of extra dimension nodes to handle multiscale models. At each extra dimension node, the detailed microscale structure (e.g., a C-core/Si-shell structure) can be considered. A spherical symmetry particle can be treated as a one-dimensional problem. Weak form was used to implement the extra dimension nodes method in COMSOL MULTIPHYSICS.

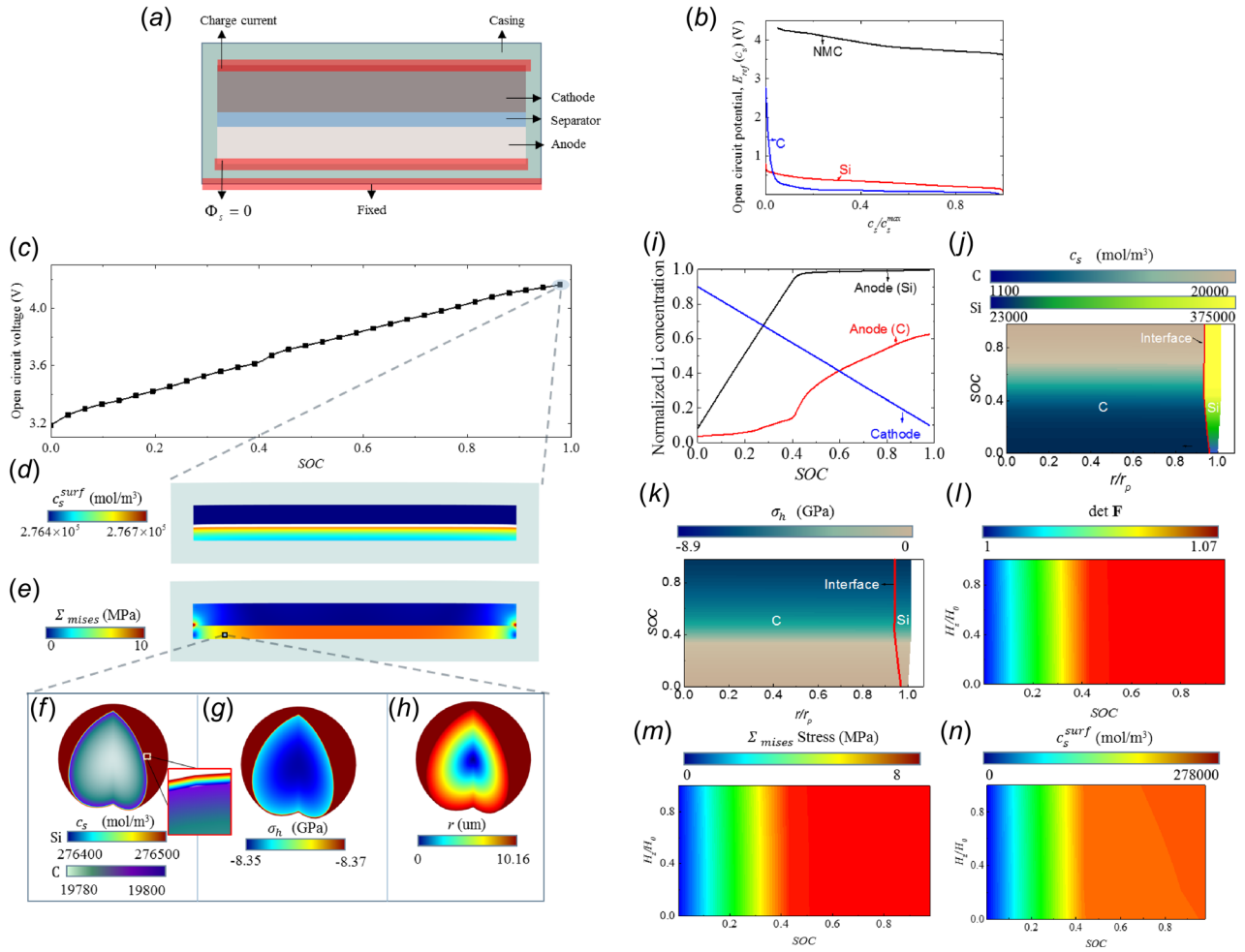

Fig. 3 Li-ion battery full cell modeling results using the present multiscale and multiphysics models: (*a*) geometry and boundary conditions of the model, (*b*) OCP curves for $LiNi_{1/3}Mn_{1/3}Co_{1/3}O_2$ (NMC) cathode, C, and Si anodes, which are provided to the model as inputs, (*c*) simulated OCV–SOC curve of the Li-ion battery, (*d*) contour plot of surface Li concentration in the continuum scale when SOC = 0.98, (*e*) contour plot of von Mises stress in the continuum scale when SOC = 0.98, (*f*)—(*h*) Li concentration, hydrostatic stress, and radial deformation, respectively, of a C-core/Si-shell particle at one particular extra dimension node (in the microscale) chosen from (*e*), (*i*) the evolution of normalized average Li concentration (i.e., c_s^{ave}/c_s^{max}) in anode (C-core and Si-shell) and cathode as a function of SOC in the continuum scale, (*j*) contour plot of Li concentration as a function of deformed radius r/r_p of the particle and SOC in the microscale, (*k*) contour plot of the hydrostatic stress as a function of deformed radius r/r_p of the particle and SOC in the microscale, and (*l*)–(*n*) volumetric deformation, stress, and Li surface concentration in anode as a function of normalized thickness of the anode and SOC in the continuum scale, respectively

With the subscript "C" for C-core, the variables in Eqs. (20) and (21) will take the corresponding values for C-core, for example c_s will be $c_{s,C}$ and Ω will be Ω_C. For Si-shell with inner radius r_C and other radius r_p, the similar equation can be obtained as

$$\int_{r_C}^{r_p}\left(-r^2\frac{\partial c_{s,\mathrm{Si}}}{\partial t}\hat{c}_{s,\mathrm{Si}}+r^2A_{\mathrm{Si}}\frac{\partial c_{s,\mathrm{Si}}}{\partial r}\frac{\partial \hat{c}_{s,\mathrm{Si}}}{\partial r}+r^2B_{\mathrm{Si}}\frac{\partial \sigma_{h,\mathrm{Si}}}{\partial r}\frac{\partial \hat{c}_{s,\mathrm{Si}}}{\partial r}\right)dr = r^2\hat{c}_{s,\mathrm{Si}}\left(A_{\mathrm{Si}}\frac{\partial c_{s,\mathrm{Si}}}{\partial r}+B_{\mathrm{Si}}\frac{\partial \sigma_{h,\mathrm{Si}}}{\partial r}\right)\Bigg|_{r_C}^{r_p} \tag{22}$$

A_{Si} and B_{Si} will be given by Eqs. (20) and (21). At the interface of the C-core and Si-shell, the continuity condition for chemical potential is applied

$$\mu_C = \mu_{\mathrm{Si}} \quad \text{at } r = r_C \tag{23}$$

The boundary conditions and the initial conditions are

$$\frac{\partial c_{s,\mathrm{C}}}{\partial r} = 0 \quad \text{at } r = 0 \tag{24}$$

$$j_s = \frac{I}{F} \quad \text{at } r = r_p \tag{25}$$

$$c_s(r) = c_s^{\mathrm{initial}} \quad \text{at } t = 0 \tag{26}$$

Here, the intercalation current density I is passed from the electrochemical model in the continuum scale (i.e., Eq. (1)), and c_s^{initial} is the initial Li concentration in C and Si.

It should be noted that the present model does not consider the phase transformation that has been observed through in situ transmission electron microscope observations for Si anodes. This treatment can be justified for the following reasons. Si that is used in many Li-ionbatteries is amorphous Si, rather than crystalline Si that exhibits phase transformation. A recent study [44] based on a realistic battery geometry has shown that amorphous Si anode remains amorphous (i.e., one phase), and the previously reported two-phase reaction for amorphous Si is actually due to the extremely large charging rate using the in situ transmission electron microscope setup [45].

2.4 Mechanics Model in the Microscale. The mechanical model in the microscale is to solve lithiation-induced stress,

Table 1 Material and geometry parameters used in the case study

Parameters	Value	Reference
Electrochemistry in continuum scale		
Cathode thickness H_{cathode}	$60\,\mu$m	
Anode thickness H_{anode}	$40\,\mu$m	
Separator thickness $H_{\text{separator}}$	$9\,\mu$m	
Length of the battery	1 mm	
Volume fraction of solid in cathode $\varepsilon_{s,\text{cathode}}$	0.6	
Volume fraction of liquid in cathode $\varepsilon_{e,\text{cathode}}$	0.23	
Volume fraction of solid in anode $\varepsilon_{s,\text{anode}}$	0.59	
Volume fraction of liquid anode $\varepsilon_{e,\text{anode}}$	0.24	
Electrical conductivity of cathode $\kappa_{s,\text{cathode}}$	100 S/m	[46]
Electrical conductivity of anode $\kappa_{s,\text{anode}}$	1 S/m	[47,48]
Initial Li^+ concentration in electrolyte, C_e^{initial}	$1000\,\text{mol/m}^3$	[49]
Diffusion coefficient in electrolyte D_e	$7.5 \times 10^{-11}\,\text{m}^2/\text{s}$	[49]
Conductivity of electrolyte κ_e	$f(C_e)$	[49]
Transference data t_+	0.363	[49]
Mechanics in the continuum scale		
Modulus of cathode E_{cathode}	182 MPa	[50]
Modulus of anode E_{anode}	140 MPa	[50]
Modulus of separator $E_{\text{separator}}$	262 MPa	[51]
Electrochemistry in the microscale		
Maximum Li concentration in Si $c_{s,\text{Si}}^{\max}$	$278,000\,\text{mol/m}^3$	[47]
Maximum Li concentration in C, $c_{s,C}^{\max}$	$31,507\,\text{mol/m}^3$	[48]
Diffusion coefficient in Si, D_{Si}	$1.67 \times 10^{-14}\,\text{m}^2/\text{s}$	[52,53]
Diffusion coefficient C, D_C	$1 \times 10^{-9}\,\text{m}^2/\text{s}$	[54]
Open circuit potential of C, $E_{\text{ref}}(c_{s,C})$	Fig. 3(*b*)	[48]
Open circuit potential of Si, $E_{\text{ref}}(c_{s,\text{Si}})$	Fig. 3(*b*)	[47]
Open circuit potential of NMC, $E_{\text{ref}}(c_{s,\text{NMC}})$	Fig. 3(*b*)	[46]
Radius of C/Si composite, r_p	$10\,\mu$m	
Si volume ratio, γ	0.1	
Radius of C, r_C	$\sqrt[3]{1-\gamma}\,r_p$	
Radius of NMC	$6\,\mu$m	
Mechanics in the microscale		
Partial molar volume of Si Ω_{Si}	$9 \times 10^{-6}\,\text{m}^3/\text{mol}$	[52]
Partial molar volume of C Ω_C	$3.17 \times 10^{-6}\,\text{m}^3/\text{mol}$	[55]
Modulus of Si (Li_xSi)	$E_{\text{Si}}(c_{s,\text{Si}})$	[44]
Modulus of C (Li_xC_6)	$19.25 + 82.23\,x$ GPa	[55]

strain, and displacement fields. For a spherical particle, the equilibrium equation becomes

$$\frac{d\sigma_r}{dr} + \frac{2}{r}(\sigma_r - \sigma_\theta) = 0 \tag{27}$$

Linear elasticity is considered here, and the constitutive relation gives

$$\sigma_{ij} = 2G\varepsilon_{ij} + \lambda\varepsilon_{kk}\delta_{ij} - \frac{\alpha E}{1-2\nu}\Delta c_s \delta_{ij} \tag{28}$$

where G is the shear modulus, λ is the Lamé constant, α is the coefficient of lithiation expansion (Eq. (11)), E is the elastic modulus, and $\Delta c_s = c_s - c_s^{\text{initial}}$. Concentration-dependent moduli have been considered. For the C-core and Si-shell structure, the following boundary conditions are used:

$$u_{r,C} \quad \text{is bounded} \quad \text{at} \quad r = 0 \tag{29}$$

$$\begin{aligned} u_{r,\text{Si}} &= u_{r,\text{C}} \quad \text{at} \quad r = r_\text{C} \\ \sigma_{h,\text{Si}} &= \sigma_{h,\text{C}} \quad \text{at} \quad r = r_\text{C} \end{aligned} \tag{30}$$

$$u_{r,\text{Si}} = (\sqrt[3]{\det\mathbf{F}} - 1)r_p \quad \text{at} \quad r = r_p \tag{31}$$

The similar extra dimension nodes method is used to implement the mechanics model in the microscale in COMSOL MULTIPHYSICS shown in Fig. 2.

3 Case Study

Now, this multiscale and multiphysics model will be applied to study a full cell. The cell consists of C-core/Si-shell composite anode, NMC cathode, a separator, $LiFP_6$ electrolyte, and a cell casing (Fig. 3(*a*)). The material and geometry parameters are summarized in Table 1. Among these parameters, Fig. 3(*b*) provides the OCPs $E_{\text{ref}}(c_{s,\text{Si}})$, $E_{\text{ref}}(c_{s,C})$, and $E_{\text{ref}}(c_{s,\text{NMC}})$, for Si, C, and NMC electrodes Boukamp et al., respectively, which will be used in the continuum scale (Eq. (3)) and the microscale electrochemical model (Eq. (20)). Solid mechanics and Li-ion battery modules are used. Given that NMC cathode has small deformation during charge/discharge, the coupling between electrochemistry and mechanics is not considered and the NMC cathode was modeled by the classical pseudo two-dimensional electrochemical model [41,42] and the lithiation eigen expansion was not considered. In total, 2244 quadrilateral elements were applied on the continuum scale and 16 edge elements were applied on the microscale. The multiscale and multiphysics model was applied on a C-core/Si-shell anode (this model can also be used for Si-core/C-shell anode) with 0.1 Si/C volume ratio. 0.1 C charging rate was used in the simulation. The casing material is 70-μm in thickness and has elastic modulus 1.5 GPa (similar to aluminum laminated polyethylene film). The mechanical boundary conditions were applied on the bottom of the battery full cell to prevent rigid-body motions. Distinct components of the battery cell (i.e., anode, cathode, separator, casing) were connected through sharing nodes.

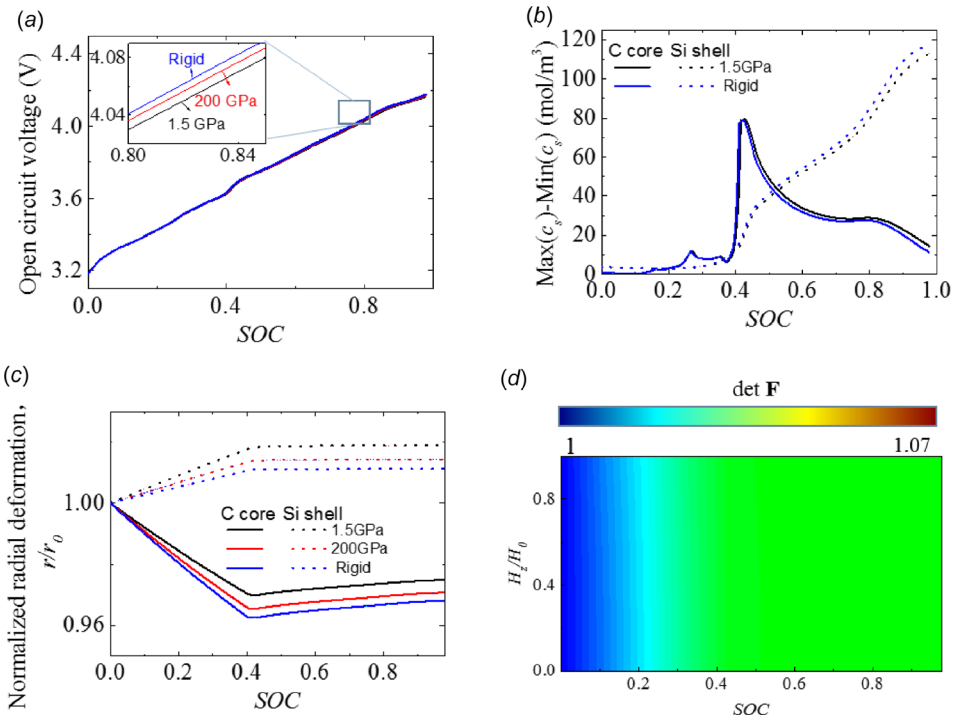

Fig. 4 Effects of mechanical constraints on the battery performance: (*a*) simulated OCV–SOC curves, (*b*) difference in Li concentration in Si-shell and C-core, and (*c*) the average radial deformation of particles in microscale for different mechanical constraints, and (*d*) contour plot of volumetric expansion of the anode in the continuum scale as a function of SOC and normalized thickness of anode for the ideally rigid casing condition

The simulation results are given in Figs. 3(*c*)–3(*n*). Figure 3(*c*) shows the charging profile with initial open circuit voltage (OCV) 3.2 V when the state of charge (SOC) equals zero. The initial voltage 3.2 V (SOC = 0) is related to the initial Li concentration of anode and cathode. The charging stops (i.e., SOC = 1) when the normalized Li concentration $c_{s,\mathrm{NMC}}/c_{s,\mathrm{NMC}}^{\max}$ drops to 5% (Fig. 3(*b*)), and the OCV at the fully charged state reaches 4.2 V. Figures 3(*d*) and 3(*e*) show the contour plots of surface Li concentration c_s^{surf} and von Mises stress Σ_{Mises} in the continuum scale when SOC = 0.98. Since a slow change rate 0.1 C is used, the surface Li concentration c_s^{surf} is fairly uniform in both anode and cathode. Note that c_s^{surf} near the separator is slightly higher because of the gradient of the electrolyte concentration C_e. Given a C-core/Si-shell structure, the surface Li concentration c_s^{surf} is actually $c_{s,\mathrm{Si}}^{\mathrm{surf}}$ and almost achieves the maximum Li concentration in Si $c_{s,\mathrm{Si}}^{\max} = 278,000\,\mathrm{mol/m^3}$ (Table 1), which suggests that the anode almost reaches its lowest potential. In Fig. 3(*e*), because of the constraint from the casing, all members in a battery cell have stress caused by the lithiation eigen expansion of the anode. The stress level in anode is much larger than that in cathode. The stress concentration occurs at the edge of the separator because of the swelling of the anode and larger stiffness of the separator. Figures 3(*f*)–3(*h*) show the Li concentration, stress, radial deformation, respectively, of a C-core/Si-shell particle at one extra dimension node (in the microscale) chosen in Fig. 3(*e*). As seen in Fig. 3(*f*), Li concentrations in Si-shell and C-core are fairly uniform but $c_{s,\mathrm{Si}}$ almost achieve $c_{s,\mathrm{Si}}^{\max}$ while $c_{s,\mathrm{C}}$ is only about 60% of the fully charged state $c_{s,\mathrm{C}}^{\max}$. The explanation is that since Si-shell and C-core have the same potential at the C/Si interface (Eq. (23)), higher OCP of Si than C (Fig. 3(*b*)) leads to higher Li concentration in Si than that in C. The hydrostatic stress in the microscale is approximately uniform (Fig. 3(*g*)). Figure 3(*h*) shows that there is about 1.6% increase in the diameter of the particle and radius increases from 10 μm to 10.16 μm. To further explain Fig. 3(*f*), Fig. 3(*i*) shows the evolution of normalized average Li concentration (i.e., $c_s^{\mathrm{ave}}/c_s^{\max}$) in anode (C-core and Si-shell) and cathode as a function of SOC in the continuum scale. During charging (SOC increasing), Li concentration in cathode drops linearly, while Li concentrations in C and Si are nonlinear. Under the same SOC, the normalized average Li concentration in Si is much higher than that in C because Si has higher OCP than C (Fig. 3(*b*)). The average Li concentration in Si almost increases to the maximum value $c_{s,\mathrm{Si}}^{\max}$ at 40% SOC. For C, the Li concentration is quite low before 40% SOC and then increases with a higher rate afterward. It is apparent that Li^+ is charged to Si then to C. Even at the fully charged state (SOC = 100%), C does not achieve its maximum capacity. It is caused by the inappropriate ratio between cathode and anode. One possible solution to this problem is to have more cathode materials or less C anode.

To show the coupled deformation and Li concentration in the microscale, Fig. 3(*j*) provides a contour plot of Li concentration as a function of deformed radius r/r_p of the particle and SOC. It is apparent that Li concentration is fairly uniform in each material and Si has a much higher Li concentration than C at any SOCs. A clear interface between C-core and Si-shell can be observed. The swelling of Si-shell initially squeezes C-core at low SOC and then saturates when SOC reaches 40%, followed by small swelling of C. The total expansion of Si is similar with the experiment developed by Liu et al. [56]. Figure 3(*k*) shows a contour plot of hydrostatic stress as a function of radial deformation and SOC. It is apparent that stress increases with SOC and has a uniform distribution along the radial direction for all SOCs.

Figures 3(*l*)–3(*n*) show the volumetric deformation, stress, and Li surface concentration in anode as a function of normalized thickness of the anode and SOC in the continuum scale. These three figures all suggest that at a given SOC, there is no apparent gradient in the thickness direction. The deformation, stress, and Li concentration increase with SOC and saturate at about 40% SOC.

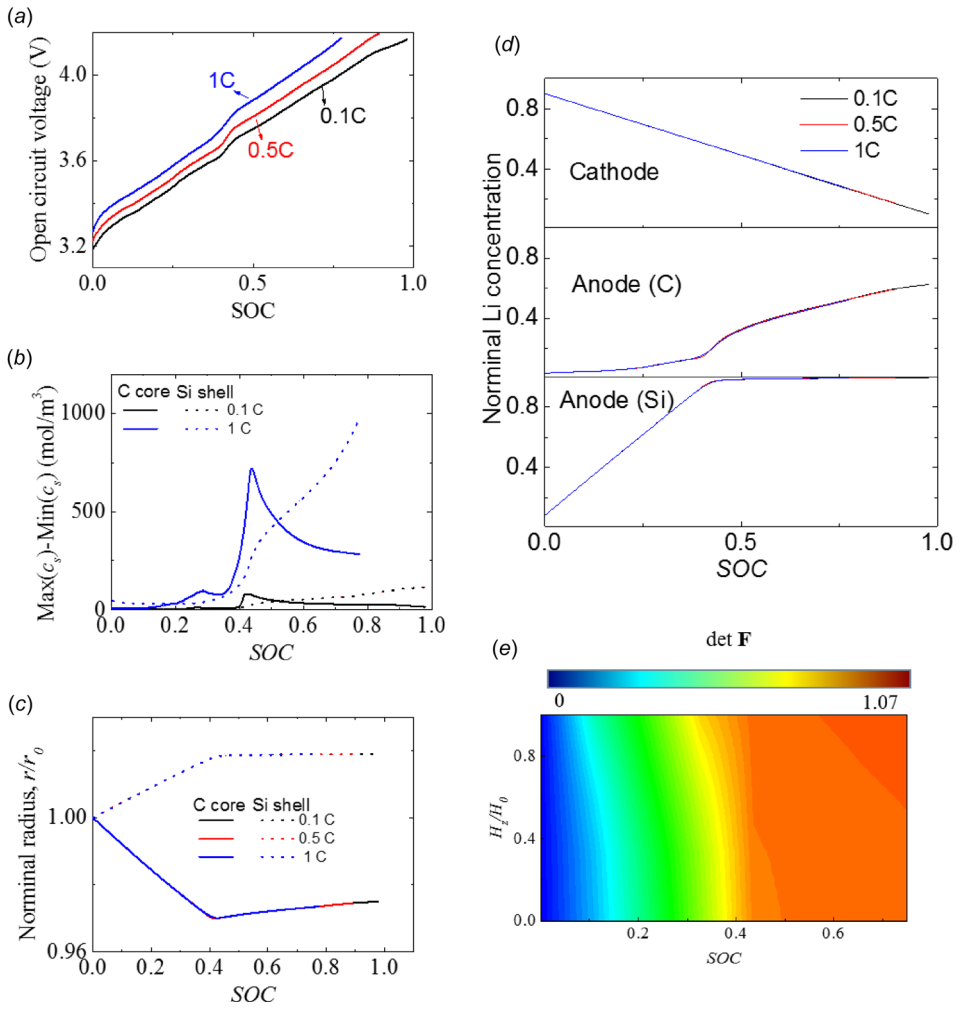

Fig. 5 Effects of charging rate on the battery performance: (*a*) simulated OCV–SOC curves, (*b*) difference in Li concentration in Si-shell and C-core, (*c*) the average radial deformation of particles in microscale, and (*d*) average Li concentration in anode and cathode for different charging rates, and (*e*) contour plot of volumetric swelling of anode as a function of SOC and normalized anode thickness for 1 C charging rate

After that, Si-shell has been fully charged and C-core has smaller capacity and swelling, which barely change these variables.

4 Effects of Mechanical Constraints, Electrochemical Boundary Conditions, and Microscale Particles on Battery Performance

In this section, we will utilize the developed model to perform multiscale and multiphysics battery design by studying the effects of mechanical constraints, electrochemical boundary conditions, and microscale particles on the battery performance. Since the developed model is multiscale, we can study the factors from the macroscopic scale (i.e., mechanical constraints and electrochemical boundary conditions) and from the microscale (i.e., particle composition). The emphasis of this section will be on the coupling among different multiphysics fields.

4.1 The Effects of Mechanical Constraints. Stainless steel, aluminum, and aluminum laminated polyethylene films are the most commonly used materials for battery casing. Different casing materials and thickness lead to different mechanical constraints for the battery cell. In this section, we studied the effects of different casing materials, e.g., aluminum laminated polyethylene film (modulus 1.5 GPa), steel (modulus 200 GPa), and ideally rigid materials, with thickness of 0.07 mm, on the multiphysics response of battery cells. 0.1 C charging rate was used. Si/C ratio in anode was 0.1.

Figure 4(*a*) shows the voltage–SOC curves for different mechanical constraints. It seems that there are very small differences for different casing materials. At SOC = 80%, only 0.25% difference in voltage is observed between using ideally rigid materials and aluminum laminated polyethylene films as the casing materials. Different mechanical constraints will cause different stress levels in the electrodes, which will in turn affect the diffusion and thus Li surface concentration and voltage. Under the same SOC, the battery cell with ideally rigid casing has a slightly higher voltage than other casing conditions because of the slightly higher stress in electrodes, which leads to relatively larger gradient in Li concentration between surface and interior of the particles. This can be further explained by Fig. 4(*b*) showing the difference in Li concentration in Si-shell and C-core. Figure 4(*b*) shows that rigid constraint leads to larger spatial difference of Li concentration in Si-shell. Figures 4(*a*) and 4(*b*) suggest that mechanical constraints seem to play a very minor role in the electrochemical performance. However, two points must be emphasized here. First, the current model has only one layer of anode and one layer of cathode, while practical battery full cells have

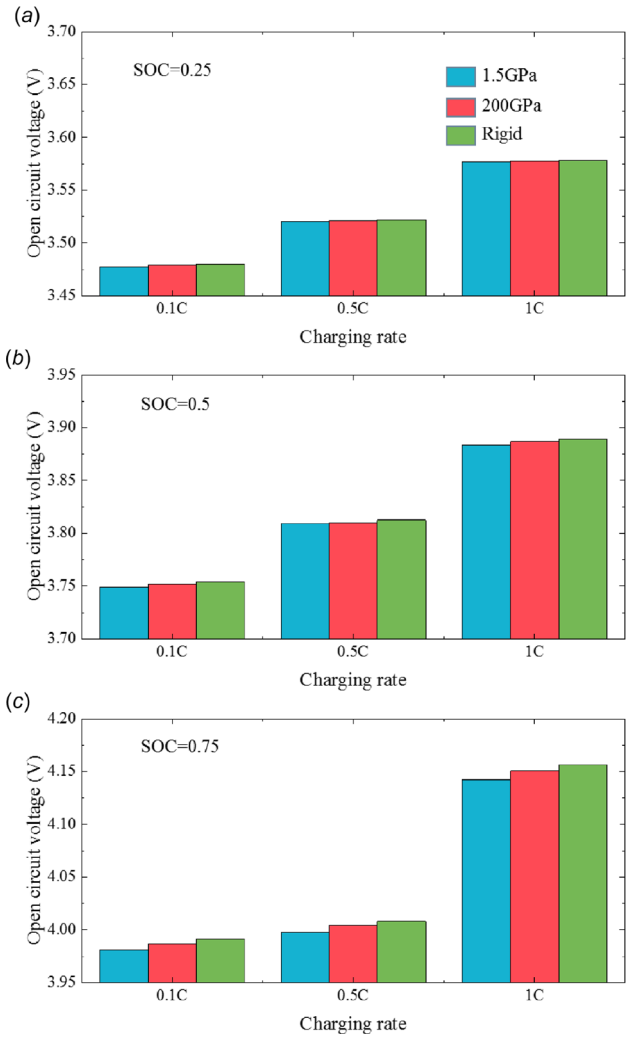

Fig. 6 Coupled effects of mechanical constraints and charging rates on the battery performance. Simulated OCV for different mechanical constraints and charging rates under different SOC, with (*a*) SOC = 0.25, (*b*) SOC = 0.5, and (*c*) SOC = 0.75.

tens of layers of anode and cathode, which will cause stress concentration and magnify the effects of mechanical constrains on voltage. Thus, a few percent differences in voltage using different mechanical constraints are expected for real battery cells. Second, a few percent differences in voltage cannot be neglected because small voltage difference may lead to accumulated effects in battery packs and for many charging/discharging cycles. This result actually suggests that for battery design, the effect of mechanical constraints on the voltage of battery cells should be considered.

Figure 4(*c*) shows the average radial deformation of particles in microscale, normalized by the initial radius of C-core and Si-shell. Mechanical constraints lead to apparent difference in the microscale deformation. With less constraint (modulus 1.5 GPa), Si-shells tend to swell outward and do not severally squeeze the C-core inward. With more constraint (ideally rigid), Si-shells have to squeeze the C-core inward to accommodate the volumetric deformation. Figure 4(*d*) gives the contour plot of volumetric expansion of the anode in the continuum scale as a function of SOC and normalized thickness of anode for the ideally rigid casing condition. As compared with the similar contour plot in Fig. 3(*l*) for aluminum laminated polyethylene casing with 107% volumetric swelling, rigid casing has less volumetric swelling of 104%.

4.2 Effects of Charging Rate. Figure 5 shows the effects of charging rate using aluminum laminated polyethylene as the casing material. Figure 5(*a*) shows voltage–SOC curves for three charging rates, 0.1 C, 0.5 C, and 1 C. As expected, charging rate has strong effects on voltage–SOC curves. At the same SOC, higher charging rate leads to higher voltage. The mechanism is that charging rate affects Li^+ diffusion, thus surface concentration, and eventually voltage of the cell. When compared with Fig. 4(*a*), it is obvious that charging rate has a more prominent effect than mechanical constraint. The larger spatial gradients in Li concentration for both C-core and Si-shell under 1 C charging rate are shown in Fig. 5(*b*), as compared with that for 0.1 C charging rate.

Figure 5(*c*) shows the average radial deformation of all particles in microscale, normalized by the initial radius of C-core or Si-shell. Surprisingly, there is no difference in the average particle deformation among different charging rates we studied (i.e., below 1 C charging rate). This is because that the average Li concentrations in anode and cathode are almost unchanged with different charging rate (Fig. 5(*d*)), though there is spatial gradient in the radial direction (Fig. 5(*b*)). Under the same SOC, there will be the same amount of Li stored in cathode or anode and does not depend on charging rate. Thus, the charging rate only affects the spatial gradient but not the average deformation. Figure 5(*e*) shows the contour plot of volumetric swelling of anode as a function of SOC and normalized anode thickness for 1 C charging rate. When compared with Fig. 3(*l*) (0.1 C charging rate), it can be found that they have the same maximum volumetric swelling, while different spatial gradients (i.e., larger swelling close to the separator for 1 C charging rate) were present.

Figure 6 shows the combined effects of mechanical constraints and charging rates. In Fig. 6(*a*), for lower SOC = 0.25, the influences of mechanical constraints at different charging rate are all very small. With the increasing of SOC (0.5 for Fig. 6(*b*) and 0.75 for Fig. 6(*c*)), the mechanical constraints seem to play a more important role for higher charging rate. This result suggests that the contribution of mechanical constraints on electrochemical performance many need more thorough studies for the development of fast-charging batteries since small voltage variation for a battery pack with many cells poses challenges on power management.

4.3 Effect of Si/C Ratio and Mechanical Constraints. The present method is now applied to study the effects of Si/C ratio in the microscale on the electrochemical performance in the continuum scale. Aluminum laminated polyethylene was used as the casing material, and 0.1 C charging rate was used. Though the Si/C ratio was changed in the simulation, the thickness of cathode and anode kept constant. Figure 7(*a*) shows that with the increasing of Si/C ratio from 0.1 to 0.4 (this model was not used for a higher Si/C ratio, because the extreme large deformation leads to no convergence of the simulation), under the same SOC, the voltage drops. Because of the high OCP of Si (Fig. 3(*b*)), the OCV drops for high Si/C ratio. Figure 7(*b*) shows the average radial deformation of all particles in microscale, normalized by the initial radius of C-core or Si-shell for different Si/C ratio. As expected, anode with high Si/C ratio has larger radial deformation. When Si/C ratio is 0.4, the deformation of Si-shell does not reach saturation and C-core experiences about 10% compression in the radial direction. The average Li concentrations in cathode and anode are shown in Fig. 7(*c*). It is found that with increasing Si/C ratio, for Si/C ratio 0.4, Si-shell only achieved about 50% of its maximum capacity and C-core was just lightly charged. This result suggests that for high Si/C ratio, more cathode materials should be provided to accommodate higher capacity of the anode.

We also studied the coupling effects of mechanical constraints (in the continuum scale) and Si/C ratio (in the microscale) on the OCV of the battery cell (in the continuum scale), as shown in Fig. 8. There are two main findings. The first one is that higher

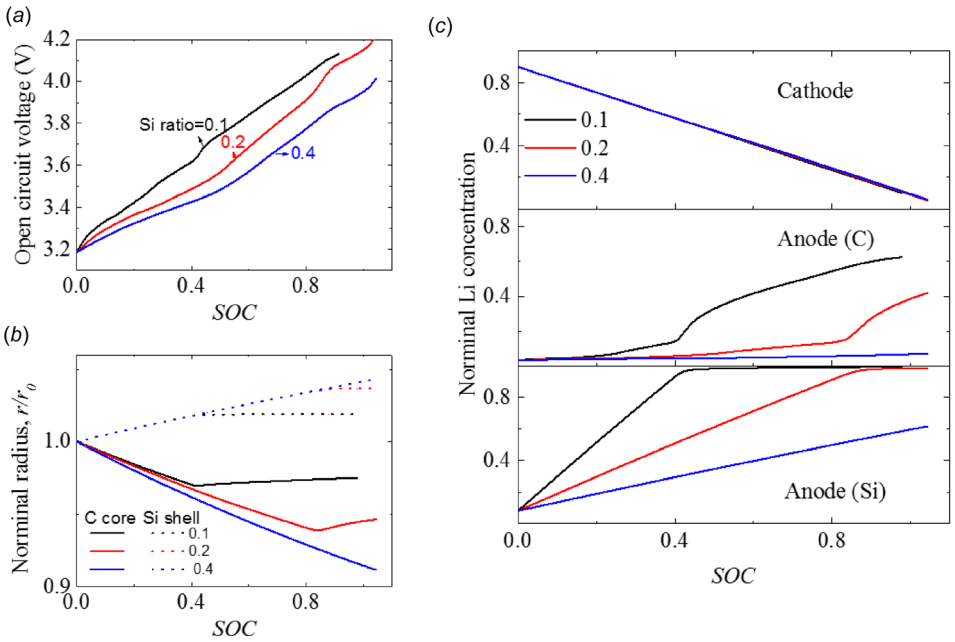

Fig. 7 Effects of Si/C ratio on the battery performance: (*a*) simulated OCV–SOC curves, (*b*) the average radial deformation of particles in microscale, and (*c*) normalized average Li concentration in anode and cathode for different charging rates

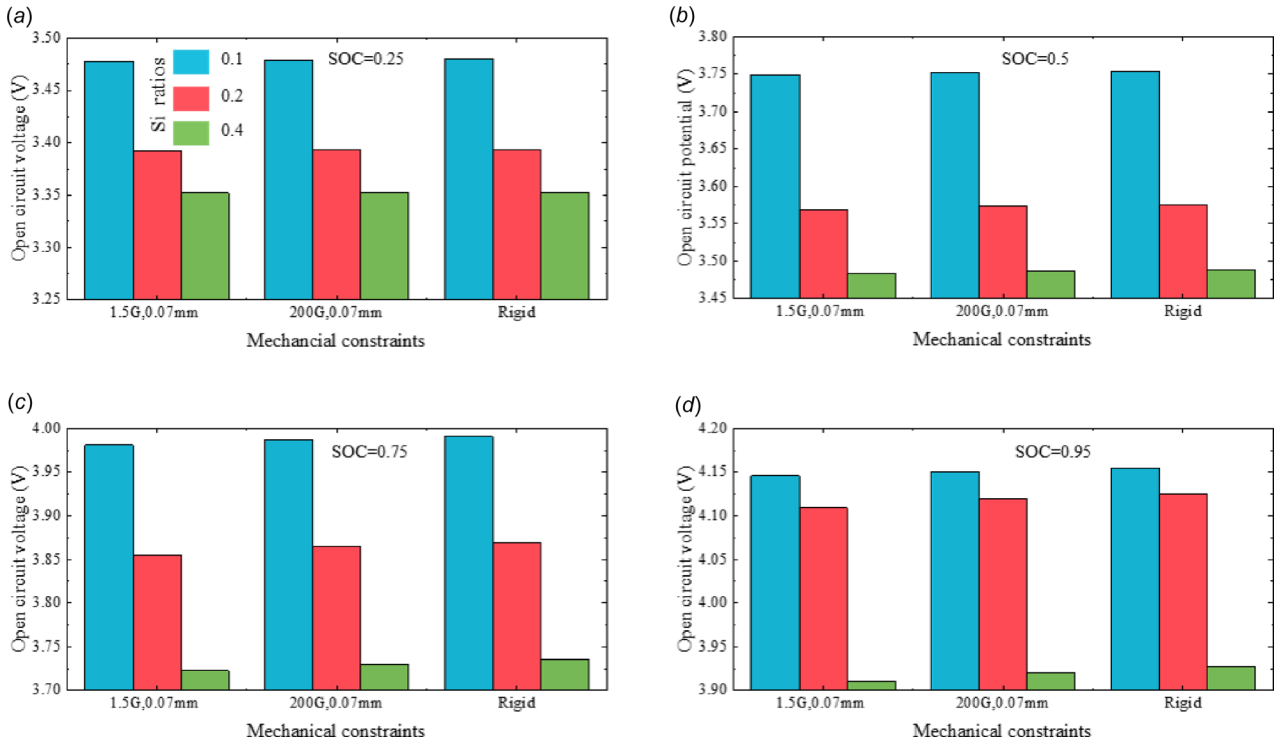

Fig. 8 Coupled effects of mechanical constraints and Si/C ratios on battery performance. Simulated OCV for different mechanical constraints and Si/C ratios under different SOC, with (*a*) SOC = 0.25, (*b*) SOC = 0.5, (*c*) SOC = 0.75, and (*d*) SOC = 0.95.

Si/C ratio leads to lower OCVs for all studied mechanical constraints, which is consistent with that in Fig. 7(*a*). The second one is that high Si/C ratio enlarges the effects of mechanical constraints on voltage. For example, at SOC = 0.95 in Fig. 8(*d*), the voltage difference between the ideally rigid constraint and aluminum laminated polyethylene increases from 0.2% to 0.4%. This results future shows the importance of mechanical constraints on the development of high-capacity and fast-charging battery cells and packs.

5 Conclusions

A simultaneous multiscale and multiphysics model to study the coupled electrochemistry and mechanics in the continuum battery

cell level and the microscale particle level was developed and numerically implemented. In the continuum scale, the porous electrode theory and the classical mechanics model were applied. In the microscale, the specific particle structure (e.g., Si-shell and C-core) has been incorporated into the model and the large deformation was considered for Si-containing anode. The extra dimension nodes method was used for the multiscale modeling. This model was implemented in COMSOL MULTIPHYSICS. This model was demonstrated to study the effects of mechanical constraints, charging rate, and Si/C ratio, on the electrochemical performance. This model can provide a powerful tool to perform multiscale and multiphysics design on Li-ion batteries, from the particle level to cell level.

Moreover, this model can be extended to consider more important aspects in the multiscale and multiphysics behavior of Li-ion batteries. For example, the binder materials have not been explicitly considered in the present model, which can be included in the microscale model through another coating layer on the particle, and thus the interfacial debonding and the effect of binder modulus can be captured. Another aspect that the present model did not capture yet is the plastic deformation of the electrodes (in the continuum scale) and the particles (in the microscale). Plasticity in the continuum scale [57,58] can be readily integrated to the model. Though challenging, to incorporate the plasticity in the particle scale [20,59], the entire mechanics model in the microscale needs to be redeveloped (via weak form). Further developments can be conducted based on the present model to study more practically important problems for Li-ion battery cells and packs.

Funding Data

- Chinese Government Scholarship (201706020109, Funder ID. 10.13039/501100010890).
- National Science Foundation (Great Wall Motor, Inc. through the I/UCRC program funded, Funder ID. 10.13039/100000001).
- State Key Laboratory of Explosion Science and Technology (KFJJ17-13M, Funder ID. 10.13039/501100011349).
- The National Key Research and Development Program of China (2017YFB0103703, Funder ID. 10.13039/501100002855).

References

[1] Boukamp, B. A., Lesh, G. C., and Huggins, R. A., 1981, "All-Solid Lithium Electrodes With Mixed-Conductor Matrix," J. Electrochem. Soc., **128**(4), pp. 725–729.

[2] Di Leo, C. V., Rejovitzky, E., and Anand, L., 2015, "Diffusion-Deformation Theory for Amorphous Silicon Anodes: The Role of Plastic Deformation on Electrochemical Performance," Int. J. Solids Struct., **67–68**, pp. 283–296.

[3] Wang, X. J., Fan, F. F., Wang, J. W., Wang, H. R., Tao, S. Y., Yang, A., Liu, Y., Chew, H. B., Mao, S. X., Zhu, T., and Xia, S. M., 2015, "High Damage Tolerance of Electrochemically Lithiated Silicon," Nat. Commun., **6**, p. 8417.

[4] Ding, B., Li, X., Zhang, X., Wu, H., Xu, Z., and Gao, H., 2015, "Brittle Versus Ductile Fracture Mechanism Transition in Amorphous Lithiated Silicon: From Intrinsic Nanoscale Cavitation to Shear Banding," Nano Energy, **18**, pp. 89–96.

[5] Kuruba, R., Datta, M. K., Damodaran, K., Jampani, P. H., Gattu, B., Patel, P. P., Shanthi, P. M., Damle, S., and Kumta, P. N., 2015, "Guar Gum: Structural and Electrochemical Characterization of Natural Polymer Based Binder for Silicon–carbon Composite Rechargeable Li-Ion Battery Anodes," J. Power Sources, **298**, pp. 331–340.

[6] Yoon, D.-E., Hwang, C., Kang, N.-R., Lee, U., Ahn, D., Kim, J.-Y., and Song, H.-K., 2016, "Dependency of Electrochemical Performances of Silicon Lithium-Ion Batteries on Glycosidic Linkages of Polysaccharide Binders," ACS Appl. Mater. Interfaces, **8**(6), pp. 4042–4047.

[7] Xie, Y., Li, J., and Yuan, C., 2014, "Multiphysics Modeling of Lithium Ion Battery Capacity Fading Process With Solid-Electrolyte Interphase Growth by Elementary Reaction Kinetics," J. Power Sources, **248**, pp. 172–179.

[8] Shi, D. H., Xiao, X. R., Huang, X. S., and Kia, H., 2011, "Modeling Stresses in the Separator of a Pouch Lithium-Ion Cell," J. Power Sources, **196**(19), pp. 8129–8139.

[9] Chan, C. K., Peng, H. L., Liu, G., McIlwrath, K., Zhang, X. F., Huggins, R. A., and Cui, Y., 2008, "High-Performance Lithium Battery Anodes Using Silicon Nanowires," Nat. Nanotechnol., **3**(1), pp. 31–35.

[10] Ma, H., Cheng, F. Y., Chen, J., Zhao, J. Z., Li, C. S., Tao, Z. L., and Liang, J., 2007, "Nest-Like Silicon Nanospheres for High-Capacity Lithium Storage," Adv. Mater., **19**(22), pp. 4067–4070.

[11] Wang, X. Y., Wen, Z. Y., Liu, Y., and Wu, X. W., 2009, "A Novel Composite Containing Nanosized Silicon and Tin as Anode Material for Lithium Ion Batteries," Electrochim. Acta, **54**(20), pp. 4662–4667.

[12] Si, Q., Hanai, K., Imanishi, N., Kubo, M., Hirano, A., Takeda, Y., and Yamamoto, O., 2009, "Highly Reversible Carbon-Nano-Silicon Composite Anodes for Lithium Rechargeable Batteries," J. Power Sources, **189**(1), pp. 761–765.

[13] Park, M. H., Kim, M. G., Joo, J., Kim, K., Kim, J., Ahn, S., Cui, Y., and Cho, J., 2009, "Silicon Nanotube Battery Anodes," Nano Lett., **9**(11), pp. 3844–3847.

[14] Bourderau, S., Brousse, T., and Schleich, D. M., 1999, "Amorphous Silicon as a Possible Anode Material for Li-Ion Batteries," J. Power Sources, **81**, pp. 233–236.

[15] Yu, C., Li, X., Ma, T., Rong, J., Zhang, R., Shaffer, J., An, Y., Liu, Q., Wei, B. Q., and Jiang, H., 2012, "Silicon Thin Films as Anodes for High Performance Lithium Ion Batteries With Effective Stress Relaxation," Adv. Energy Mater., **2**(1), pp. 68–73.

[16] Christensen, J., and Newman, J., 2006, "Stress Generation and Fracture in Lithium Insertion Materials," J. Solid State Electrochem., **10**(5), pp. 293–319.

[17] Gao, Y. F., and Zhou, M., 2011, "Strong Stress-Enhanced Diffusion in Amorphous Lithium Alloy Nanowire Electrodes," J. Appl. Phys., **109**(1), p. 014310.

[18] Cui, Z. W., Gao, F., and Qu, J. M., 2012, "A Finite Deformation Stress-Dependent Chemical Potential and Its Applications to Lithium Ion Batteries," J. Mech. Phys. Solids, **60**(7), pp. 1280–1295.

[19] Yang, X. G., Bauer, C., and Wang, C. Y., 2016, "Sinusoidal Current and Stress Evolutions in Lithium-Ion Batteries," J. Power Sources, **327**, pp. 414–422.

[20] Bower, A. F., Guduru, P. R., and Sethuraman, V. A., 2011, "A Finite Strain Model of Stress, Diffusion, Plastic Flow, and Electrochemical Reactions in a Lithium-Ion Half-Cell," J. Mech. Phys. Solids, **59**(4), pp. 804–828.

[21] Yang, H., Fan, F., Liang, W., Guo, X., Zhu, T., and Zhang, S., 2014, "A Chemo-Mechanical Model of Lithiation in Silicon," J. Mech. Phys. Solids, **70**, pp. 349–361.

[22] Di Leo, C. V., Rejovitzky, E., and Anand, L., 2014, "A Cahn–Hilliard-Type Phase-Field Theory for Species Diffusion Coupled With Large Elastic Deformations: Application to Phase-Separating Li-Ion Electrode Materials," J. Mech. Phys. Solids, **70**, pp. 1–29.

[23] Huang, S., Fan, F., Li, J., Zhang, S., and Zhu, T., 2013, "Stress Generation During Lithiation of High-Capacity Electrode Particles in Lithium Ion Batteries," Acta Mater., **61**(12), pp. 4354–4364.

[24] Qi, Y., Xu, Q. C., and Van der Ven, A., 2012, "Chemically Induced Crack Instability When Electrodes Fracture," J. Electrochem. Soc., **159**(11), pp. A1838–A1843.

[25] Klinsmann, M., Rosato, D., Kamlah, M., and McMeeking, R. M., 2016, "Modeling Crack Growth During Li Insertion in Storage Particles Using a Fracture Phase Field Approach," J. Mech. Phys. Solids, **92**, pp. 313–344.

[26] Hu, Y. H., Zhao, X. H., and Suo, Z. G., 2010, "Averting Cracks Caused by Insertion Reaction in Lithium-Ion Batteries," J. Mater. Res., **25**(6), pp. 1007–1010.

[27] DeLuca, C. M., Maute, K., and Dunn, M. L., 2011, "Effects of Electrode Particle Morphology on Stress Generation in Silicon During Lithium Insertion," J. Power Sources, **196**(22), pp. 9672–9681.

[28] Purkayastha, R. T., and McMeeking, R. M., 2012, "An Integrated 2-D Model of a Lithium Ion Battery: The Effect of Material Parameters and Morphology on Storage Particle Stress," Comput. Mech., **50**(2), pp. 209–227.

[29] Cheng, Y. T., and Verbrugge, M. W., 2009, "Evolution of Stress Within a Spherical Insertion Electrode Particle Under Potentiostatic and Galvanostatic Operation," J. Power Sources, **190**(2), pp. 453–460.

[30] Zhao, K. J., Pharr, M., Vlassak, J. J., and Suo, Z. G., 2010, "Fracture of Electrodes in Lithium-Ion Batteries Caused by Fast Charging," J. Appl. Phys., **108**(7), p. 045004.

[31] Zhou, W., 2015, "Effects of External Mechanical Loading on Stress Generation During Lithiation in Li-Ion Battery Electrodes," Electrochim. Acta, **185**, pp. 28–33.

[32] Mendoza, H., Roberts, S. A., Brunini, V. E., and Grillet, A. M., 2016, "Mechanical and Electrochemical Response of a $LiCoO_2$ Cathode Using Reconstructed Microstructures," Electrochim. Acta, **190**, pp. 1–15.

[33] Kim, S., Wee, J., Peters, K., and Huang, H. Y. S., 2018, "Multiphysics Coupling in Lithium-Ion Batteries With Reconstructed Porous Microstructures," J. Phys. Chem. C, **122**(10), pp. 5280–5290.

[34] Wu, W., Xiao, X., Huang, X., and Yan, S., 2014, "A Multiphysics Model for the in Situ Stress Analysis of the Separator in a Lithium-Ion Battery Cell," Comput. Mater. Sci., **83**, pp. 127–136.

[35] Liu, B. H., Zhao, H., Yu, H. L., Li, J., and Xu, J., 2017, "Multiphysics Computational Framework for Cylindrical Lithium-Ion Batteries Under Mechanical Abusive Loading," Electrochim. Acta, **256**, pp. 172–184.

[36] Zhao, K., Pharr, M., Cai, S., Vlassak, J. J., and Suo, Z., 2011, "Large Plastic Deformation in High-Capacity Lithium-Ion Batteries Caused by Charge and Discharge," J. Am. Ceram. Soc., **94**, pp. s226–s235.

[37] Bower, A. F., and Guduru, P., 2012, "A Simple Finite Element Model of Diffusion, Finite Deformation, Plasticity and Fracture in Lithium Ion Insertion Electrode Materials," Modell. Simul. Mater. Sci. Eng., **20**(4), p. 045004.

[38] Wu, W., Xiao, X. R., Wang, M., and Huang, X. S., 2014, "A Microstructural Resolved Model for the Stress Analysis of Lithium-Ion Batteries," J. Electrochem. Soc., **161**(5), pp. A803–A813.

[39] Wang, M., Xiao, X., and Huang, X., 2017, "A Multiphysics Microstructure-Resolved Model for Silicon Anode Lithium-Ion Batteries," J. Power Sources, **348**, pp. 66–79.

[40] Wu, L., Wen, Y., and Zhang, J., 2016, "Three-Dimensional Finite Element Study on Li Diffusion Induced Stress in FIB-SEM Reconstructed $LiCoO_2$ Half Cell," Electrochim. Acta, **222**, pp. 814–820.
[41] Doyle, C. M., Fuller, T. F., and Newman, J. S., 1993, "Modeling of Galvanostatic Charge and Discharge of the Lithium/Polymer/Insertion Cell," J. Electrochem. Soc., **140**(6), pp. 1526–1533.
[42] Doyle, C. M., 1995, "Design and Simulation of Lithium Rechargeable Batteries," Ph.D. thesis, Lawrence Berkeley National Laboratory, Berkeley, CA.
[43] COMSOL Multiphysics, 2015, "COMSOL AB," v. 5.2, Stockholm, Sweden.
[44] Wang, X., Singh, S. S., Ma, T., Lv, C., Chawla, N., and Jiang, H. Q., 2017, "Quantifying Electrochemical Reactions and Properties of Amorphous Silicon in a Conventional Lithium-Ion Battery Configuration," Chem. Mater., **29**(14), pp. 5831–5840.
[45] McDowell, M. T., Lee, S. W., Harris, J. T., Korgel, B. A., Wang, C., Nix, W. D., and Cui, Y., 2013, "In Situ TEM of Two-Phase Lithiation of Amorphous Silicon Nanospheres," Nano Lett., **13**(2), pp. 758–764.
[46] Zheng, W. D., Shui, M., Shu, J., Gao, S., Xu, D., Chen, L. L., Feng, L., and Ren, Y. L., 2013, "GITT Studies on Oxide Cathode $LiNi1/3Co1/3Mn1/3O_2$ Synthesized by Citric Acid Assisted High-Energy Ball Milling," Bull. Mater. Sci., **36**(3), pp. 495–498.
[47] Sethuraman, V. A., Srinivasan, V., and Newman, J., 2013, "Analysis of Electrochemical Lithiation and Delithiation Kinetics in Silicon," J. Electrochem. Soc., **160**(2), pp. A394–A403.
[48] Srinivasan, V., and Newman, J., 2004, "Design and Optimization of a Natural Graphite/Iron Phosphate Lithium-Ion Cell," J. Electrochem. Soc., **151**(10), pp. A1530–A1538.
[49] Doyle, M., Newman, J., Gozdz, A. S., Schmutz, C. N., and Tarascon, J. M., 1996, "Comparison of Modeling Predictions With Experimental Data From Plastic Lithium Ion Cells," J. Electrochem. Soc., **143**(6), pp. 1890–1903.
[50] Xu, J., Liu, B., and Hu, D., 2016, "State of Charge Dependent Mechanical Integrity Behavior of 18650 Lithium-Ion Batteries," Sci. Rep., **6**, p. 21829.
[51] Xu, J., Wang, L. B., Guan, J., and Yin, S., 2016, "Coupled Effect of Strain Rate and Solvent on Dynamic Mechanical Behaviors of Separators in Lithium Ion Batteries," Mater. Des., **95**, pp. 319–328.
[52] Wang, M., Xiao, X., and Huang, X., 2016, "Study of Lithium Diffusivity in Amorphous Silicon Via Finite Element Analysis," J. Power Sources, **307**, pp. 77–85.
[53] Johari, P., Qi, Y., and Shenoy, V. B., 2011, "The Mixing Mechanism During Lithiation of Si Negative Electrode in Li-Ion Batteries: An Ab Initio Molecular Dynamics Study," Nano Lett., **11**(12), pp. 5494–5500.
[54] Park, M., Zhang, X. C., Chung, M. D., Less, G. B., and Sastry, A. M., 2010, "A Review of Conduction Phenomena in Li-Ion Batteries," J. Power Sources, **195**(24), pp. 7904–7929.
[55] Qi, Y., Guo, H. B., Hector, L. G., and Timmons, A., 2010, "Threefold Increase in the Young's Modulus of Graphite Negative Electrode During Lithium Intercalation," J. Electrochem. Soc., **157**(5), pp. A558–A566.
[56] Liu, X. H., Zhong, L., Huang, S., Mao, S. X., Zhu, T., and Huang, J. Y., 2012, "Size-Dependent Fracture of Silicon Nanoparticles During Lithiation," ACS Nano, **6**(2), pp. 1522–1531.
[57] Wen, J., Wei, Y., and Cheng, Y.-T., 2018, "Stress Evolution in Elastic-Plastic Electrodes During Electrochemical Processes: A Numerical Method and Its Applications," J. Mech. Phys. Solids, **116**, pp. 403–415.
[58] Wang, L., Yin, S., Zhang, C., Huan, Y., and Xu, J., 2018, "Mechanical Characterization and Modeling for Anodes and Cathodes in Lithium-Ion Batteries," J. Power Sources, **392**, pp. 265–273.
[59] Zhao, K., Wang, W. L., Gregoire, J., Pharr, M., Suo, Z., Vlassak, J. J., and Kaxiras, E., 2011, "Lithium-Assisted Plastic Deformation of Silicon Electrodes in Lithium-Ion Batteries: A First-Principles Theoretical Study," Nano Lett., **11**(7), pp. 2962–2967.